Kovove Mater. 60 2022 191–208
DOI: 10.31577/km.2022.3.191

Influence of nano-$Si_3N_{4(P)}$ hybridization on the mechanical and quasi-static compression behaviour of AA6082-Metakaolin composites

Renjin J. Bright[1]*, G. Selvakumar[2], P. Hariharasakthisudhan[3], M. Sumathi[4]

[1] *Department of Production Engineering, PSG College of Technology, Peelamedu, Coimbatore, Tamil Nadu, India*
[2] *Department of Mechanical Engineering, Sri Sivasubramaniya Nadar College of Engineering, Kalavakkam, Chennai, Tamil Nadu, India*
[3] *Department of Mechanical Engineering, National Engineering College, Kovilpatti, Tamil Nadu, India*
[4] *Department of Mechanical Engineering, Jeppiaar Institute of Technology, Sriperumbudur Chennai, Tamil Nadu, India*

Received 30 September 2021, received in revised form 25 May 2022, accepted 26 May 2022

Abstract

This work studies the mechanical and quasi-static compression behaviour of AA6082/Metakaolin composites hybridized with nano-silicon nitride (Si_3N_4) particles. Hybridization with nano-Si_3N_4 particles was intended to improve the ductility of the composites. The composites were manufactured using an ultrasonication-assisted stir casting process. The weight fraction (wt.%) of Metakaolin was maintained as 7.5 wt.%, and the nano-Si_3N_4 particles were added by varying their wt.% from 0.5 to 2.5 % at the increment of 0.5 %. A premixing technique was adopted to blend the Metakaolin and Si_3N_4 reinforcements to improve their wettability and dispersion in the matrix. The tensile properties and microhardness of the composites improved with the incorporation of nano-Si_3N_4 particles up to 1 wt.%. The compressive strength was higher for the AMC with 1.5 wt.% Si_3N_4. The workability of hybrid composites was studied by the cold upsetting process where the composites were subjected to quasi-static compression.

K e y w o r d s: hybrid aluminum composites, Metakaolin, silicon nitride, ultrasonication, tensile properties, workability

1. Introduction

AA6xxx series alloys and composites find applications in aeronautical, automobile, and construction industries to produce components such as brakes, valves, racing bike frames, etc. The properties such as strength, hardness, and wear resistance of aluminium alloy are increased by producing the composites with suitable ceramic particles as reinforcement. The features which limit the application of the composites are the processing cost and the cost of reinforcement. The utilization of industrial wastes, agro-wastes, and natural minerals as alternative reinforcement materials in composites would reduce the cost of reinforcements [1]. However, these composites possess lower material properties when compared to the composites developed with synthetic ceramic reinforcements [2]. The hybrid composites could address this issue by maintaining the cost-effective materials as primary reinforcement and synthetic ceramic material as secondary reinforcement. Bodunrin et al. [3] reported that the hybrid composites showed superior properties to the composites with single reinforcement and the monolithic alloy. Alaneme et al. [4] employed quarry dust particles as reinforcements along with SiC in the AA6063 matrix and noted the enhancement of tensile strength. The aluminium composites developed by Kanth et al. [5] with AA7075 as matrix and silicon carbide (SiC) and fly ash particles as reinforcements possessed a finer grain structure than the monolithic aluminium alloy AA7075. The finer grain structure possessed by these composites caused the increase in hardness, ultimate strength, and yield strength. Quader et al. [6] processed AA6061 composites with alumina (Al_2O_3) and red mud particles as reinforcements and observed improved tensile strength and

*Corresponding author: e-mail address: renjin1990@gmail.com

hardness. Kumar et al. [7] studied the mechanical behaviour of AA7075-SiC-Bamboo Leaf Ash metal matrix composites and noted the improvement in tensile properties and hardness.

From various literature, it has been observed that the ductility of aluminium metal matrix composites with particulate reinforcements degraded while showing improvement in other mechanical properties. The development of aluminium matrix composites without degrading the ductility is always a research interest under concern. Nano-scale reinforcement particles has improved the strength and wear behaviour of the composites without degrading the ductility [8, 9]. Wang et al. [10] stated that Si_3N_4 nanoparticles, reinforced with AZ91 magnesium alloy, offered better ductility and fracture toughness. Mattli et al. [11] observed improvement in tensile strength and microhardness without any degradation in ductility of aluminium composites with nano Si_3N_4 particles as reinforcements. The ductility of AA6061 composites improved while nano Si_3N_4 particles were reinforced along with micro Al_2O_3 and graphite particles [12]. Arik [13] also stated similar results while reinforcing Si_3N_4 particles in the Al matrix. The dispersion of nano-sized reinforcement particles in the matrix encourages the Orowan strengthening mechanism compared to micro-sized reinforcement particles and improves the ductility [14]. The high cost of the nano-scale reinforcement particles is a limiting factor for their utilization in the large-scale production of nanocomposite materials. However, this problem could be curtailed to a certain extent by employing the nano-scale particles as a secondary reinforcement in small quantities and along with a cost-effective primary reinforcement.

The proper dispersion of reinforcement particles in the matrix plays an important role in the mechanical properties of the composites [15]. The ultrasonication-assisted stir casting method could be potentially used for processing the aluminium composites with nano-sized particulate reinforcements [16]. The ultrasonication-assisted stir casting process could reduce the issues such as agglomeration and improper wettability observed while processing aluminium composites using conventional stir casting [17, 18].

The workability study decides the ability of a material to endure the internal stresses induced as a result of forming operations. In most of the forming processes, such as rolling, forging, swaging, etc., the state of stress and strain are measured in the localized regions in which fractures initiate. The factors such as workpiece geometry, friction at the interface of the die and workpiece, and die design parameters control these localized stresses and strains. The cold upsetting test is performed to evaluate the workability of the material in most of the research works. Narayanasamy et al. [19] investigated the cold upsetting behaviour of Al-Al_2O_3 composites developed using the powder metallurgy technique. Narayanasamy et al. [20] reported the improvement in strain hardening exponent n and strength coefficient K of Al/SiC composites with respect to the addition of SiC reinforcement. Taha et al. [21] developed aluminium composites with micro SiC particles and characterized their workability behaviour by evaluating the workability index WI. The maximum WI value signifies the maximum possible height reduction without the crack initiation. The aluminium composites prepared by the stir casting technique exhibited better workability than those processed by powder metallurgy [21].

AA6082 possesses the highest strength among the alloys in the 6xxx series and is observed to be overriding the AA6061 in major structural applications. Hybrid composites show significant research outcomes to overcome the shortcomings of composite materials. Metakaolin is an abundant ceramic material that exhibits superior strength when used as reinforcement in aluminium matrix despite the lack of ductility. The ductility of the material needs to be retained to form the material for broad applications. It is intended to improve the ductility and workability of the AA6082/Metakaolin composites by hybridizing them with Si_3N_4 nanoparticles as secondary reinforcement.

The extensive literature study shows that very few research works focused on utilizing nano-ceramic particulates as secondary reinforcement and a natural mineral like Metakaolin to produce aluminium composites. It was also noted that less attention was given to proper premixing of the hybrid reinforcements before incorporating them into the aluminium matrix. This work extends the research towards bridging the above two gaps. In this work, the weight fraction of the Metakaolin particles in AA6082/Metakaolin composite was maintained as 7.5 wt.% with reference to Bright et al. [22]. The Si_3N_4 nanoparticles were hybridized with the Metakaolin particles by adopting the premixing technique developed by Hariharasakthisudhan and Jose [12]. The composites were synthesized using ultrasonication-assisted stir casting and were subjected to mechanical characterization under the as-cast condition. The mechanical properties and workability behaviour of the composites were evaluated. The microstructural attributes of the composites were examined using Optical Microscopy (OM), Scanning Electron Microscopy (SEM), and Energy-Dispersive X-ray Spectroscopy (EDAX).

2. Materials and methodology

2.1. Materials

AA6082 was used as the matrix material for this research work. AA6082 rods were purchased from the local suppliers of aluminium alloys in Chennai, India.

Table 1. Chemical composition of AA6082 [22]

Element	Si	Cu	Mg	Mn	Fe	Ni	Zn	Ti	Cr	Al
Composition %	1.19	0.03	0.89	0.72	0.041	0.03	0.02	0.1	0.15	96.828

Table 2. Chemical composition of Metakaolin powder [22]

Constituent	SiO_2	Al_2O_3	Fe_2O_3	CaO	Na_2O	K_2O	MgO	TiO_2	P_2O_5
Composition %	51.85	43.87	0.89	0.20	0.01	0.03	0.28	1.74	0.15

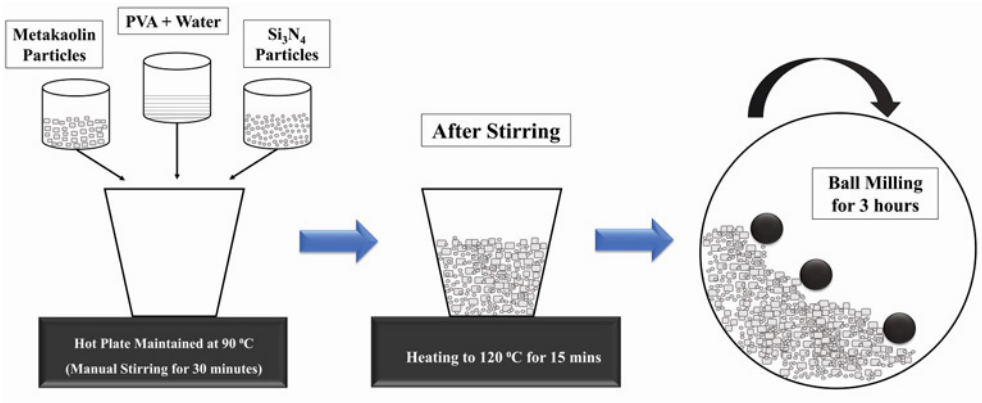

Fig. 1. Schematic representation of the premixing process.

The chemical composition of the AA6082 is shown in Table 1. Metakaolin powder with assorted particle sizes in the range of 100–200 nm and Si_3N_4 nanoparticles of size less than 50 nm were used as the reinforcement materials. The Metakaolin powder was procured from Ashwin ceramics, Chennai. The nano-Si_3N_4 powder of 99 % purity was purchased from Luoyang Tongrun Info Technology Co., Ltd., China. The density of Metakaolin powder is 2.6 g cm^{-3}, and that of Si_3N_4 powder is 3.17 g cm^{-3}. The chemical composition of the Metakaolin powder provided by the supplier is represented in Table 2.

2.2. Premixing of the reinforcements

A novel premixing method discussed by Hariharasakthisudhan and Jose [12] to produce hybrid aluminium composites was found to give better results in terms of wettability. Figure 1 portrays the schematic diagram, which explains the procedure of the premixing process.

The Metakaolin and Si_3N_4 particles were premixed before adding to the matrix. Poly Vinyl Alcohol (PVA) was used as the functionalising agent, and water was utilized as the plasticizer since PVA is soluble in water. The predetermined amount of Metakaolin particles and Si_3N_4 particles were functionalized using PVA. PVA tends to improve the binding between Metakaolin and Si_3N_4 particles. The blend of Metakaolin and Si_3N_4 particles were prepared by manual stirring for 30 min on a hot plate maintained at a temperature of 90 ℃. It was then heated to 120 ℃ for 15 min to remove the volatile content in the blend. The premixed reinforcements were then ball-milled for 3 h.

Figures 2a–d represent the SEM images of the individual reinforcement particles and the premixed reinforcements. From Fig. 2a, it could be noted that the Metakaolin particles possessed a flake-like structure with particle size within the range of 100 to 200 nm. From the Si_3N_4 particle cluster shown in Fig. 2b, it could be observed that the shape of the Si_3N_4 particles is nearly spherical, with a size range of less than 50 nm. Figures 2c,d represent the morphology of the premixed reinforcements in which the blend of flake-like Metakaolin particles and spherical Si_3N_4 particles could be observed.

Figures 3a–c illustrate the EDAX results of the reinforcement particles and the premixed reinforcements. From Fig. 3a, it can be inferred that the significant elements present in the Metakaolin particles are aluminium, silicon, and oxygen. The EDAX result of Si_3N_4 particles depicted in Fig. 3b shows silicon and nitrogen element peaks. The oxygen peak noted in the EDAX, along with silicon and nitrogen, may be attributed to the occurrence of oxidation. The EDAX result of premixed reinforcement particles is shown in

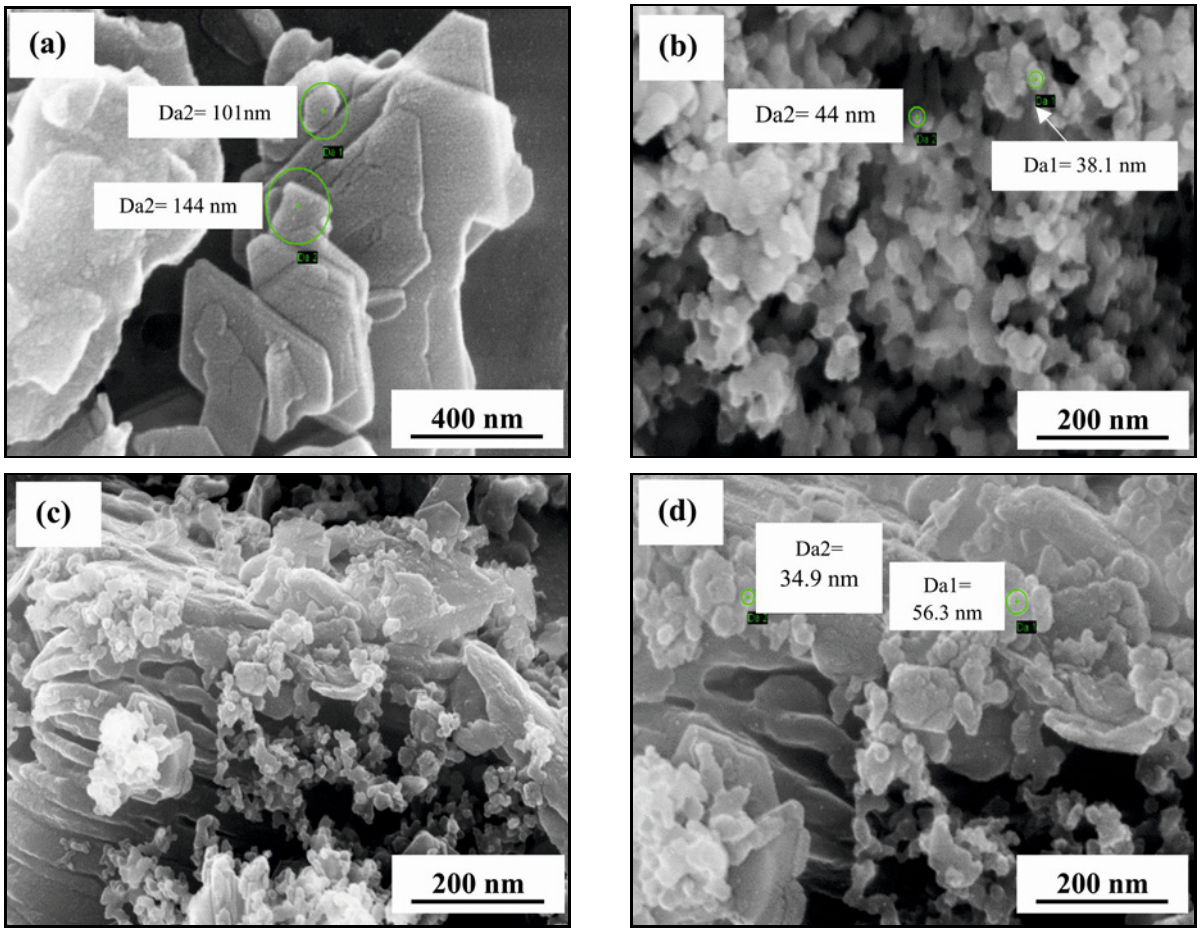

Fig. 2. SEM morphology of the reinforcements: (a) Metakaolin particles, (b) Si_3N_4 particles, (c) & (d) mixed reinforcement particles with 7.5 wt.% Metakaolin + 1 wt.% Si_3N_4.

Fig. 3c. Figure 3c confirms the peaks of aluminium, nitrogen, silicon, and oxygen.

2.3. Fabrication of hybrid composites

The schematic diagram in Fig. 4 explains the methodology adopted for processing the aluminium composites. The composites were manufactured using the ultrasonication-assisted stir casting method. The details of the ultrasonic cavitation-assisted stir casting process are explained by the authors elsewhere [22]. The power rating and output frequency of the ultrasonication setup are 2 kW and 20 kHz, respectively. The maximum temperature rating of the electric resistance furnace is noted as 1000 ℃. The ultrasonic probe is made up of titanium. The stepped type ultrasonic probe has a length of 65 mm with a diameter of 35 mm at the top portion, and the bottom portion has a length of 135 mm with a diameter of 20 mm. The AA6082 rods were placed in a graphite crucible and were melted in the furnace. The melt was mechanically stirred to obtain a uniform mixture. The reinforcement particles were pre-heated at 400 ℃ for 2 h in the muffle furnace to remove the volatile content. The reinforcement particles were progressively added from the top to the molten AA6082. The melt was stirred at 700 rpm for 10 min at different depths of the crucible using the graphite stirrer. The initial mechanical stirring helps premix the reinforcements with the aluminium alloy melt and reduces the sonication time [16, 18]. The temperature of the furnace was maintained at 750 ℃ during the stirring period [18]. After completing the initial mechanical stirring, ultrasonic cavitation was performed. During the ultrasonic cavitation, the ultrasonic generator converts the line current at 230 V to high-frequency electrical signals at 2 kHz, and the ultrasonic transducer converts the high-frequency electrical signals to mechanical vibrations of 20 kHz output frequency. The ultrasonic probe connected to the transducer transmits this vibration to the melt. The high-intensity ultrasonic vibrations break the liquid bonds of the aluminium melt and develop cavitation bubbles inside the molten material. The collapse of these cavitation bubbles due to high pressure disperses the reinforcement particles towards all parts of the melt and thus reduces agglomeration [16]. The period for the ultrasonication was maintained as 20 min for optimum con-

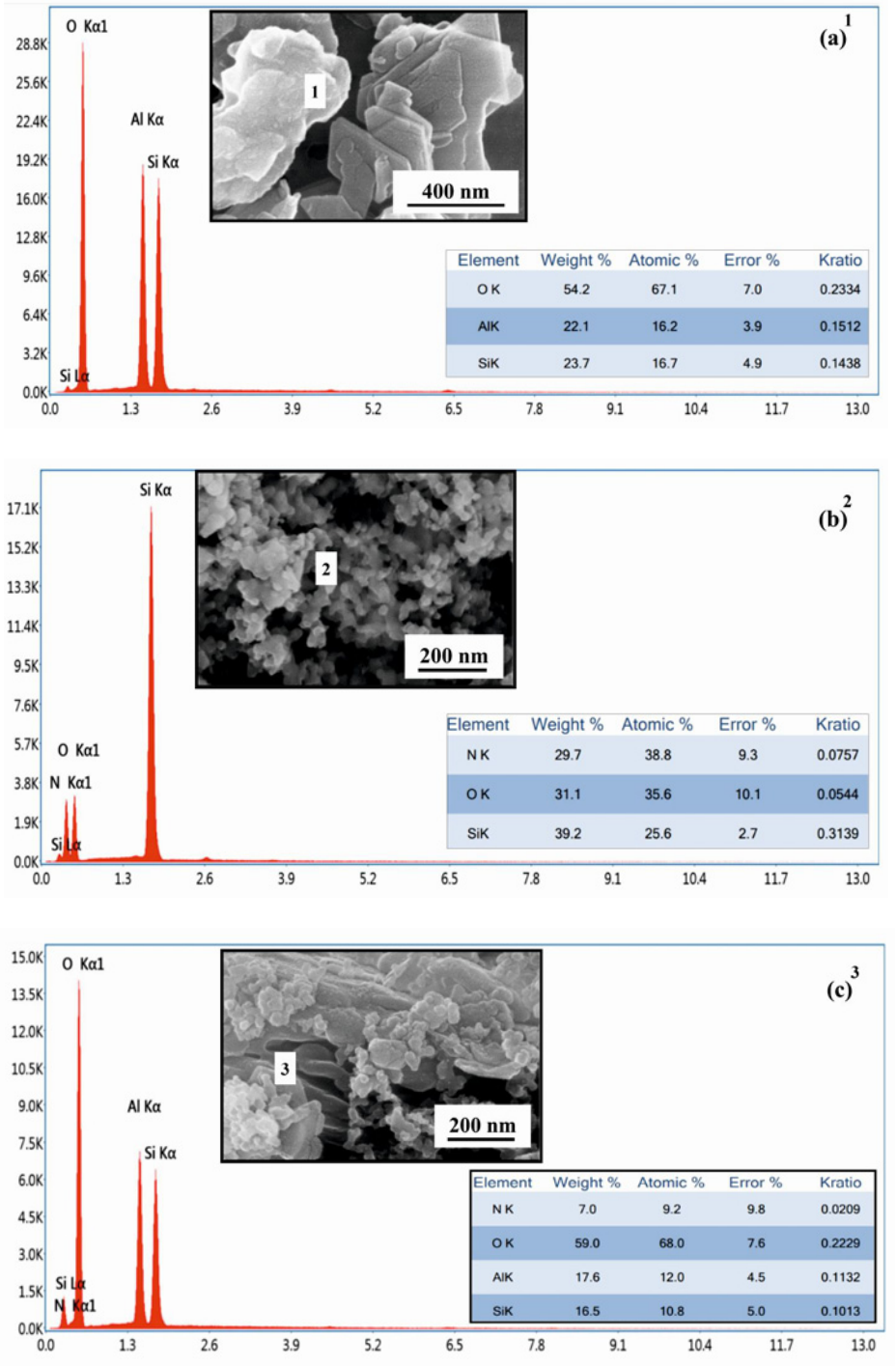

Fig. 3. EDAX result of the reinforcements: (a) Metakaolin particles, (b) Si_3N_4 particles, and (c) mixed reinforcement particles with 7.5 wt.% Metakaolin + 1 wt.% Si_3N_4.

ditions. The dispersion of Metakaolin particles in the AA6082 melt tends to increase its viscosity. Therefore, the melt temperature was raised to 850 ℃ before pouring into the die. To avoid the thermal mismatch between the melt and die, the dies were pre-heated to a temperature of 400 ℃. The prepared composites were subjected to mechanical testing under as-cast conditions. The composites were prepared by varying the amount of reinforcement particles based on the composition shown in Table 3.

2.4. Details of testing methods

The density of the hybrid composites was determined theoretically using the rule of mixture principle. The water immersion displacement method, as per

Table 3. Code and composition of the composite samples

Sample code	Metakaolin particles (wt.%)	Si_3N_4 particles (wt.%)	AA6082 (wt.%)
A0	0	0	100
A1	7.5	0	92.5
A2	7.5	0.5	92
A3	7.5	1	91.5
A4	7.5	1.5	91
A5	7.5	2	90.5
A6	7.5	2.5	90

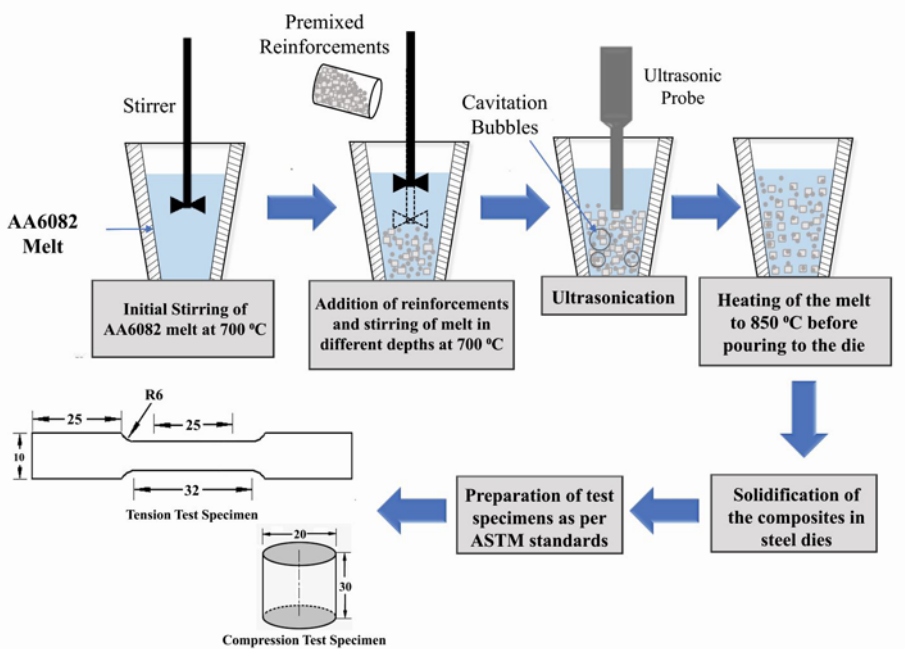

Fig. 4. Schematic representation explaining the processing of aluminium composites.

ASTM C135-2003 standard, was used to determine the experimental density [17]. The weight of the composite samples was initially measured in air and then in water. A physical weighing balance with a readability of 0.1 mg was utilized for weight measurement.

The porosity of each of the AMC samples was calculated using Eq. (1):

$$\%\text{Porosity} = \frac{\rho_{\text{theoretical}} - \rho_{\text{experimental}}}{\rho_{\text{theoretical}}}. \qquad (1)$$

All the tests were conducted at room temperature for three different samples. The tensile test was conducted as per the ASTM E8/E8M standard, and the compression test was conducted as per ASTM E9/89a standard. INSTRON-made universal testing machine (UTM) of 100 kN capacity was used to perform the tensile test. The UTM of Auto Instruments made with a capacity of 5-ton load was used to perform compression tests and workability study. The microhardness test was conducted using Vicker's hardness test according to the ASTM E92 standard. A 1 kgf load was applied on the polished surface of the composites. The dwell period of loading was maintained as 10 s. The hardness values were observed at three different locations, and the average was accounted.

3. Theoretical background

The mathematical model for evaluating the stress components and the associated strains was adopted from Narayanasamy and Pandey [23] and Narayanaswamy et al. [19]. The axisymmetric condition was applied to evaluate the stress components. The axial stress component (σ_z) was calculated using Eq. (2). The axial stress component is compressive in nature.

$$\sigma_z = \frac{\text{Load } (P)}{\text{Contact Surface Area } (A_c)}. \qquad (2)$$

Figure 5 represents the bulging behaviour of the composites during the quasi-static compression test. The

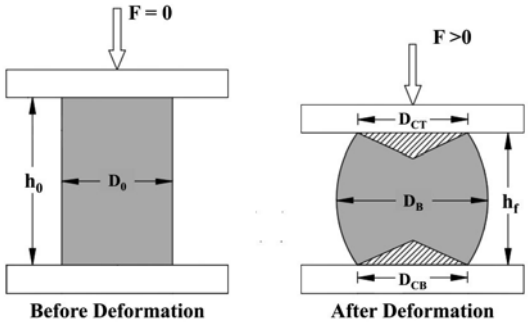

Fig. 5. Bulging behaviour during quasi-static compression.

terms 'h_0' and 'D_0' are initial height and diameter, respectively, whereas 'h_f' and 'D_B' represent the final height and bulged diameter. The term 'F' represents the applied compressive load.

The axial strain was calculated by employing the expression described by Abdel-Rahman and Sheik [24], as shown in Eq. (3):

$$\varepsilon_z = \ln\left(\frac{h_0}{h_\mathrm{f}}\right). \tag{3}$$

During the axial compression, the diameter of the cylinder increases, which increases the hoop strain until the fracture limit is reached. The hoop strain and accompanied hoop stress are tensile in nature. Narayanasamy and Pandey [24] validated expression for evaluating hoop strain as shown in Eq. (4),

$$\varepsilon_\theta = \ln\left(\frac{D_\mathrm{C}}{D_0}\right), \tag{4}$$

where D_C is the average contact diameter of the cylinder after deformation, calculated using Eq. (5) explained by Narayanasamy and Pandey [23]:

$$D_\mathrm{C} = \frac{D_\mathrm{CT} + D_\mathrm{CB}}{2}, \tag{5}$$

where D_CT represents the contact diameter at the top surface of the cylinder, and D_CB is the bottom contact surface diameter of the cylinder after the deformation.

Narayanasamy and Pandey [23] expressed the hoop strain in terms of the contact diameter D_C and bulge diameter D_C, as shown in Eq.(6):

$$\varepsilon_\theta = \ln\left[\frac{2D_\mathrm{C}^2 + D_\mathrm{C}^2}{3D_0^2}\right]. \tag{6}$$

The Poisson's ratio α, hoop stress, mean stress, and effective stress σ_eff were computed using the expressions validated by Narayanasamy et al. [19] as given by Eqs. (7), (8), (9), and (10), respectively:

$$\alpha = \frac{\varepsilon_\theta}{2\varepsilon_z}, \tag{7}$$

$$\sigma_\theta = \left(\frac{1+2\alpha}{2+\alpha}\right)\sigma_z, \tag{8}$$

$$\sigma_m = \frac{1}{3}\left(\sigma_z \pm \sigma_\theta\right), \tag{9}$$

$$\sigma_\mathrm{eff} = (0.5+\alpha)\left[3\left(1+\alpha+\alpha^2\right)\right]^{0.5}\sigma_z. \tag{10}$$

Effective stress determines the critical limit of stress at which the crack initiates.

The relationship between strain hardening exponent n and strength coefficient K is given by the Ludwik Equation shown in Eq. (11):

$$\sigma = K\varepsilon^n. \tag{11}$$

Narayanasamy et al. [20] modified Eq. (11) into Eqs. (12) and (13) to calculate instantaneous strain hardening exponent (n_i) and instantaneous strength coefficient (K_i):

$$n_i = \frac{\ln\left(\dfrac{\sigma_m}{\sigma_{m-1}}\right)}{\ln\left(\dfrac{\varepsilon_m}{\varepsilon_{m-1}}\right)}, \tag{12}$$

$$K_i = \frac{\sigma_m - \sigma_{m-1}}{\varepsilon_m^{n_i} - \varepsilon_{m-1}^{n_i}}. \tag{13}$$

The consecutive compressive loads were assumed as 1, 2, …, $m-1$, and m.

The workability index (WI) shown in Eq. (14) is defined as the ratio of initial height (h_0) to the final height (h_f) of the specimen, as explained by Taha et al. [21]:

$$\mathrm{WI} = \frac{h_0}{h_\mathrm{f}}. \tag{14}$$

The final height is the height of the specimen after the initiation of the crack in the circumference under quasi-static compression.

4. Results and discussion

4.1. Microstructure

The optical micrographs of the composite samples are shown in Figs. 6a–h. The composite samples were ground using emery paper, polished to a mirror-like finish, and etched with Keller's reagent. The yellow light filter used in the optical micrograph helped represent the grain boundaries and flaws in the composites.

Figure 6a depicts the microstructure of the unreinforced AA6082 alloy sample A0. The dark lines in the micrograph represent grain boundaries precipitated with the Mg_2Si eutectic [25]. Pores were also

observed in the microstructure. Figure 6b represents the microstructure of sample A1 with Metakaolin reinforcement. The dispersion of Metakaolin particles is observed along the grain boundaries and within the matrix. The increased darkness of the grain boundaries could be attributed to the accumulation of the Metakaolin particles [22]. Figures 6c–h represent the microstructure of the hybrid composite with both Metakaolin and Si_3N_4 particles. The darkness of the grain boundaries was observed due to the dispersion of both reinforcements. The reinforcement particles were found to be dispersed in the form of small clusters as well as isolated particles in the matrix. Figure 6d represents a refined grain structure and increased grain concentration for sample A3. The refinement in grain structure is attributed to the incorporation of nano-sized Si_3N_4 particles, as reported by Zhou et al. [26]. Figure 6e illustrates the high magnitude micrograph

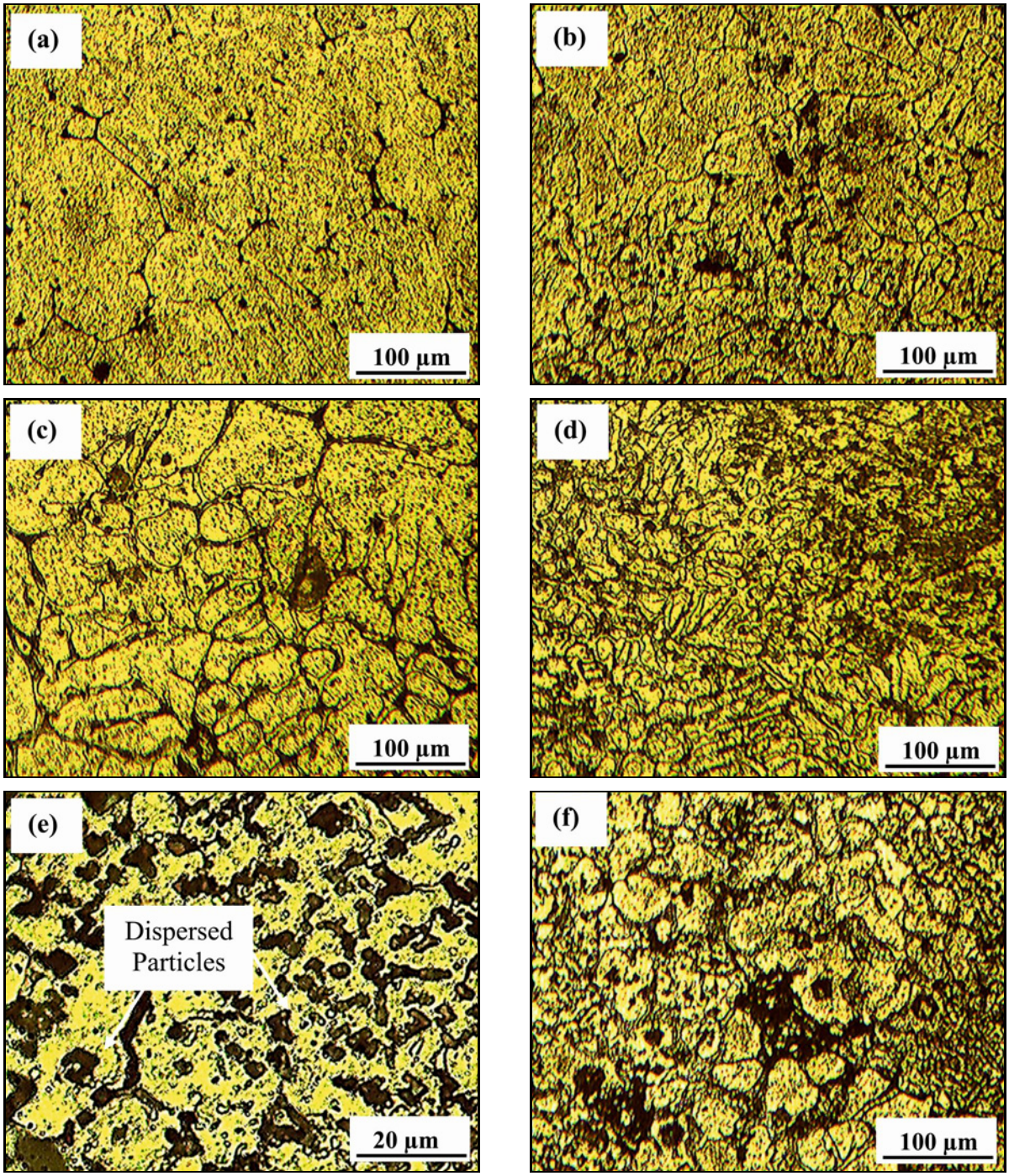

Fig. 6. Optical micrographs of composite samples: (a) A0, (b) A1, (c) A2, (d) A3, (e) A3, (f) A4.

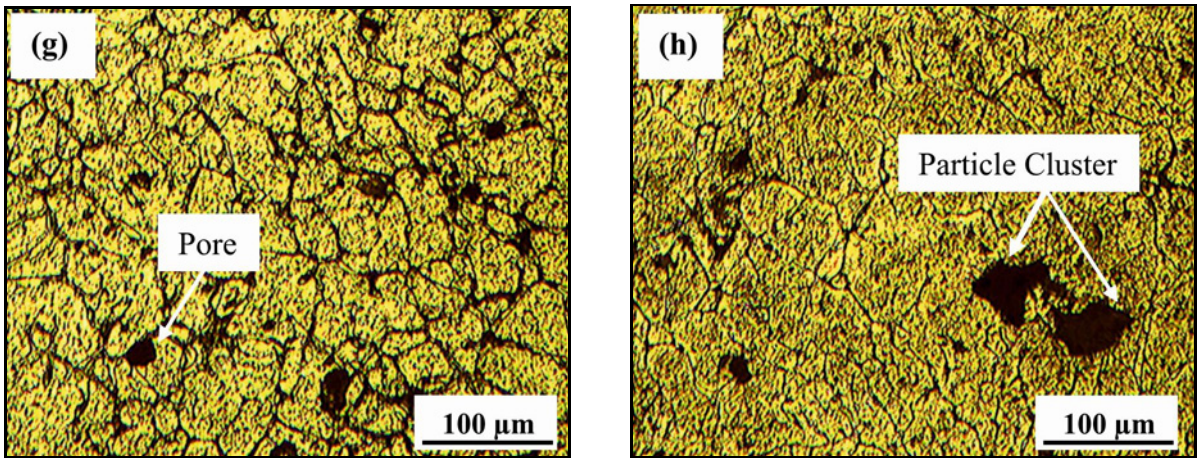

Fig. 6. Optical micrographs of composite samples: (g) A5, and (h) A6.

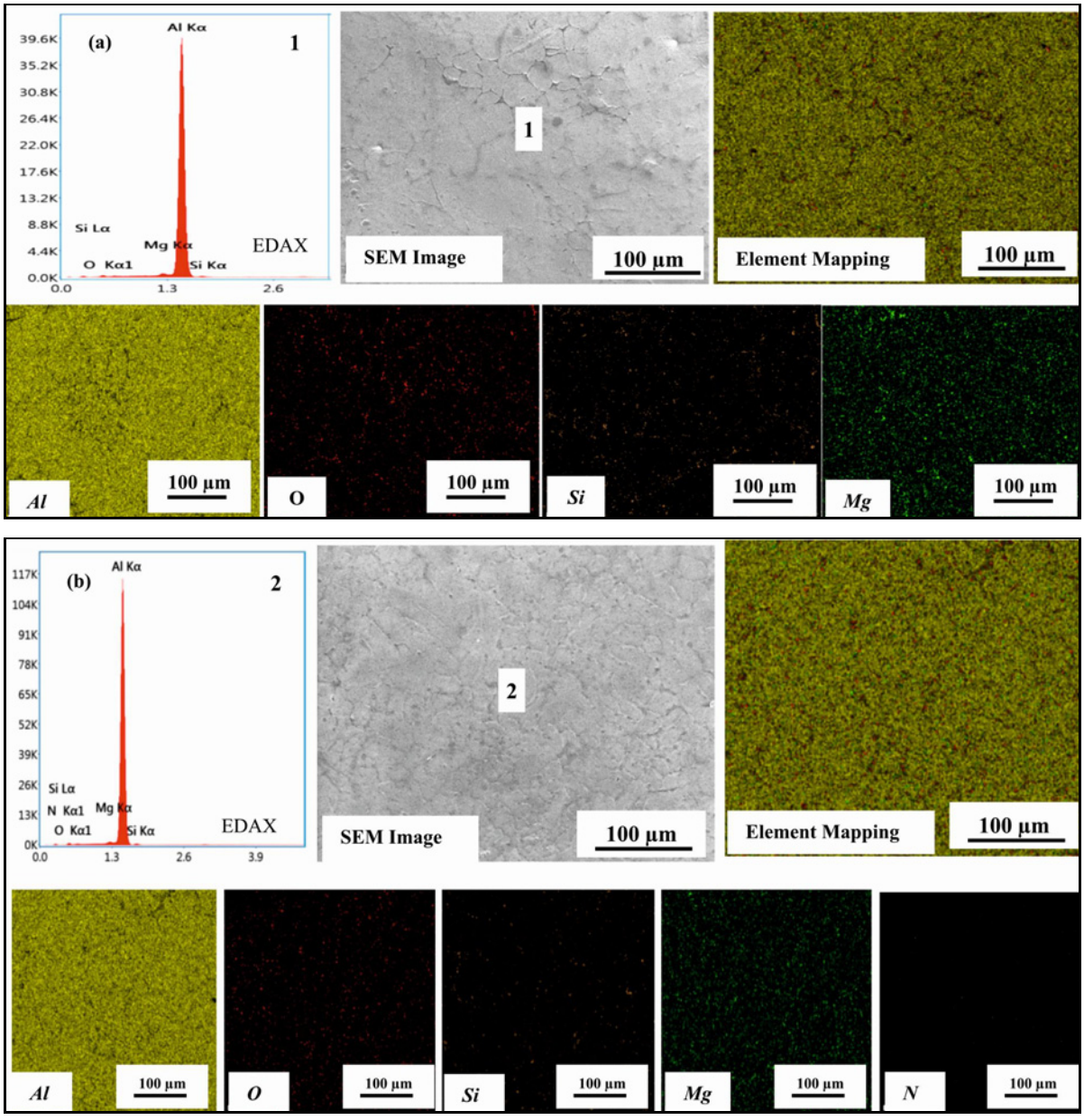

Fig. 7. SEM and EDAX results of composite samples (a) A1 and (b) A3.

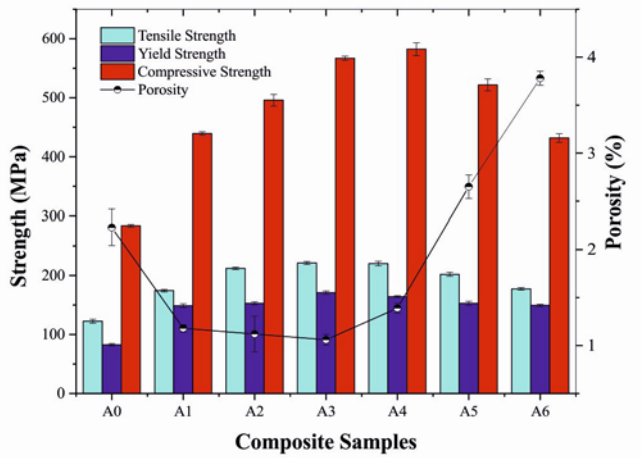

Fig. 8. Comparison of ultimate tensile strength, yield strength, and compression strength with porosity.

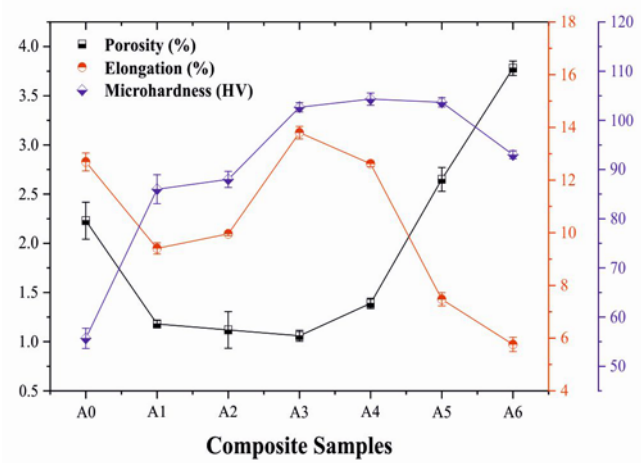

Fig. 9. Relationship between porosity, % elongation, and microhardness.

of sample A3 in which the grain boundaries are noted with the clusters of Metakaolin and Si_3N_4 particles. The clusters of particles along with grain refinement can be observed in Figs. 6f–h, which represents the microstructures of samples A5 and A6. The increased amount of nano Si_3N_4 particles in the AA6082 matrix might have triggered the occurrence of agglomeration.

Figures 7a,b depict SEM micrographs with the EDAX elemental mapping result of composite samples A1 and A3, respectively. The SEM micrographs represent well-defined grain boundaries. The grain structure was observed to be refined for sample A3 compared to A1. The EDAX result of sample A1 exhibited the peaks of elements such as Al, Mg, Si, and O. The presence of these elements confirms that the AA6082 matrix regions consist of the Metakaolin particles. EDAX result of sample A3 shown in Fig. 7b represents the peaks of elements such as Al, Mg, Si, O, and N. The presence of these elements endorsed that the AA6082 matrix regions contained the Metakaolin and Si_3N_4 particles.

4.2. Tensile and compressive properties

Figure 8 compares the tensile strength, yield strength, and compressive strength values of the composites and their relationship with the porosity. The error bars in the graph were constructed based on the standard deviation evaluated by repeating the tests for three samples. The tensile properties of the composites were noted to be improved with respect to the addition of nano-Si_3N_4 particles. The composite sample A3 exhibited the best tensile strength value (221.11 MPa), which is 79.67 % greater compared to the unreinforced alloy A0 and 26.29 % more than sample A1. The yield strength of sample A3 (168.52 MPa) also showed a similar trend. The highest compressive strength value (582.37 MPa) was observed for the hybrid composite sample A4.

Figure 9 depicts the relationship between the porosity, %elongation, and microhardness of the composite samples. The %elongation characterizes the ductility of the composites. The composite sample A3 possessed the best ductility (13.8 %). The improvement in ductility could be attributed to the presence of Si_3N_4 nanoparticles [12]. From Fig. 9, it can be perceived that the ductility of the composite was found to be lesser when the porosity was higher and vice-versa. However, the unreinforced AA6082 sample A0 possessed higher ductility even though the porosity was higher. For sample A0, the ductility was higher due to the absence of ceramic reinforcements. The ceramic reinforcements were reported to decrease the ductility of the material. As expected, a decrease in ductility was noted when the ceramic reinforcements were added. However, the influence of nano Si_3N_4 particles improved the ductility of the composites later on for samples A2 and A3. But, the composite samples A4, A5, and A6 exhibited a reduction in ductility and tensile strength due to agglomeration, which increased the particle porosity clusters [27]. From Fig. 8, it could also be noted that the microhardness improved with the reduction in porosity and reduced with respect to the increase in porosity. The best microhardness value was observed for sample A3 (86 HV). The dispersion of reinforcement particles in the matrix with minimum cluster formation could be attributed to the improvement of microhardness, as stated by Panwar and Chauhan et al. [28]. However, the increase in microhardness was not observed while the nano Si_3N_4 particles were incorporated beyond 1 wt.%. The presence of the increased amount of pores and particle clusters might have reduced the microhardness values of samples A4, A5, and A6.

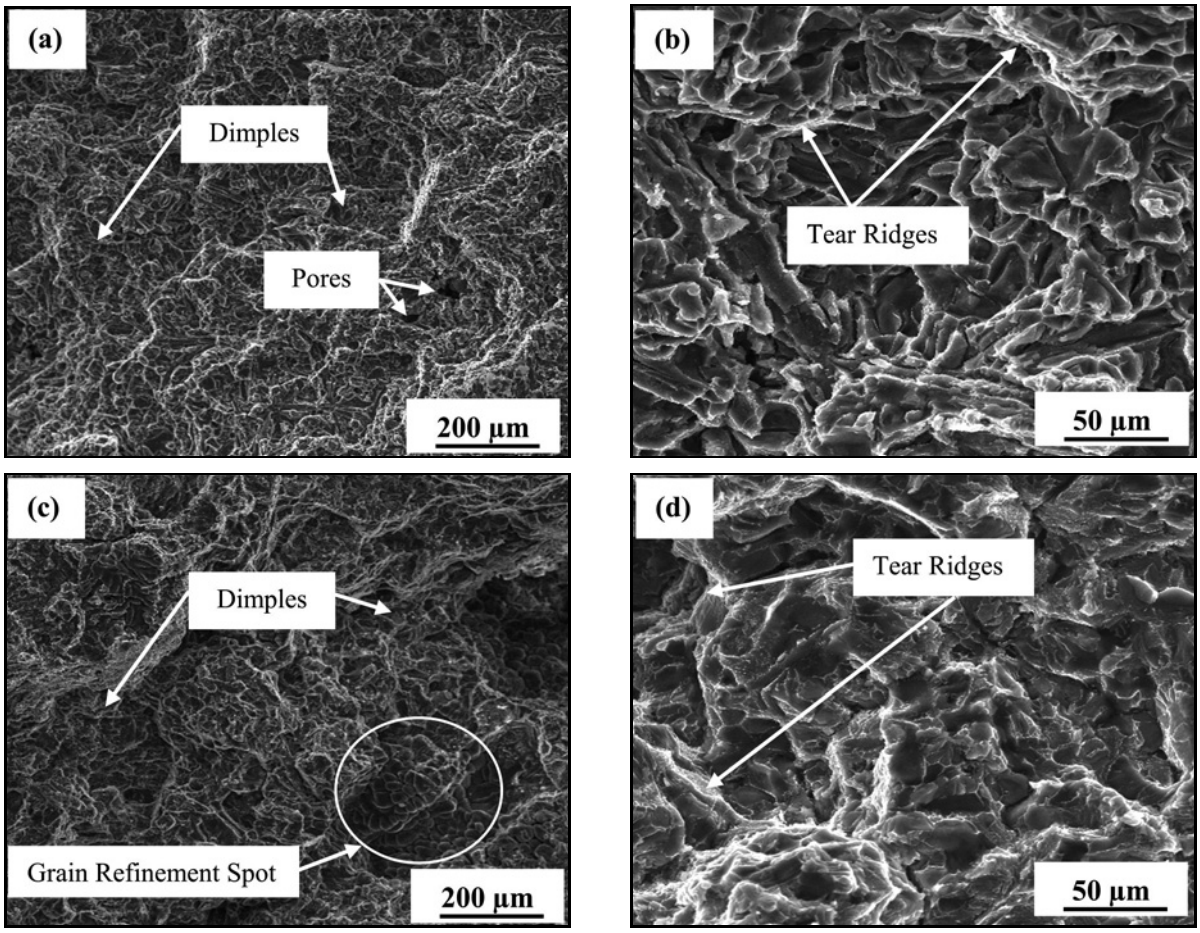

Fig. 10. Fracture surface morphology of composite samples: (a) and (b) A1, (c) and (d) A2.

The increase in mechanical properties of the composites with the addition of Si_3N_4 particles may be attributed to the dispersion strengthening mechanism. The dispersion of nano-sized Si_3N_4 and Metakaolin particles within the matrix and grain boundaries acted as a barrier for crack propagation and resulted in Orowan's strengthening mechanism. Xu et al. [29] and Raj and Thakur [30] reported similar observations. The hard Metakaolin and nano Si_3N_4 particles hinder the movement of dislocation. This trait resulted in the requirement of higher force to promote dislocation motion, which consequently increased the ultimate tensile stress and ductility of the composites. The good wettability between the reinforcement particles and the aluminium matrix might be another reason which enhanced the load transfer between the matrix and reinforcement [31]. The improvement in wettability can be attributed to the premixing process carried out to mix the Metakaolin and the nano-Si_3N_4 particles. The effect of premixing on the wettability between the reinforcements matrix could be observed from Figs. 6c,d, which show uniform dispersion of reinforcement particles within the matrix and along the grain boundaries. Incorporating nano-sized Si_3N_4 along with sub-micron-sized Metakaolin particles resulted in grain refinement by the Hall-Petch effect. The refined grain structure increased the grain boundary concentration. The increased grain boundary further extended the crack propagation path and consequently increased the ductility of the composites [26].

Figures 10 and 11 depict the SEM micrographs of the tensile fracture surface of the composites at different magnifications. Figures 10a and 10b illustrate the existence of dimples and tear ridges on the fracture surface of sample A1. The presence of a few pores could also be observed. The dimples and tear ridges represented the ductile mode of fracture. Figures 10c,d show the grain refinement along with the presence of dimples and tear ridges on the fracture surface sample A2 [25].

Figures 11a,b represent the SEM micrographs of the fracture surface of sample A3 at different magnifications. The fracture surface morphology revealed the presence of dimples, tear ridges, and mild particle clusters. Figures 11c,d exhibit the tear ridges along with the brittle facets of sample A4. Figures 11e,f portray the presence of clustered particles pulled out of

the matrix along with brittle zones and tear ridges in the fracture surface of sample A5. Figures 11a,b depict the immense amount of pores and agglomeration in the fracture surface of sample A6. Debonding the particle clusters from the matrix under tensile loading may be attributed to the presence of larger pores [12]. The presence of extended brittle facets in sample A4 represented the dominance of brittle fracture. The particle porosity clusters in samples A5 and A6, as shown in Figs. 11g,h, acted as stress raisers, leading to the catastrophic fracture. This, in turn, may be attributed to the degraded values of mechanical properties of samples A5 and A6. The fracture mechanism of all the composites was supposed to be a mixed mode of ductile and brittle fracture. The predominant ductile mode of failure observed from the SEM micrographs

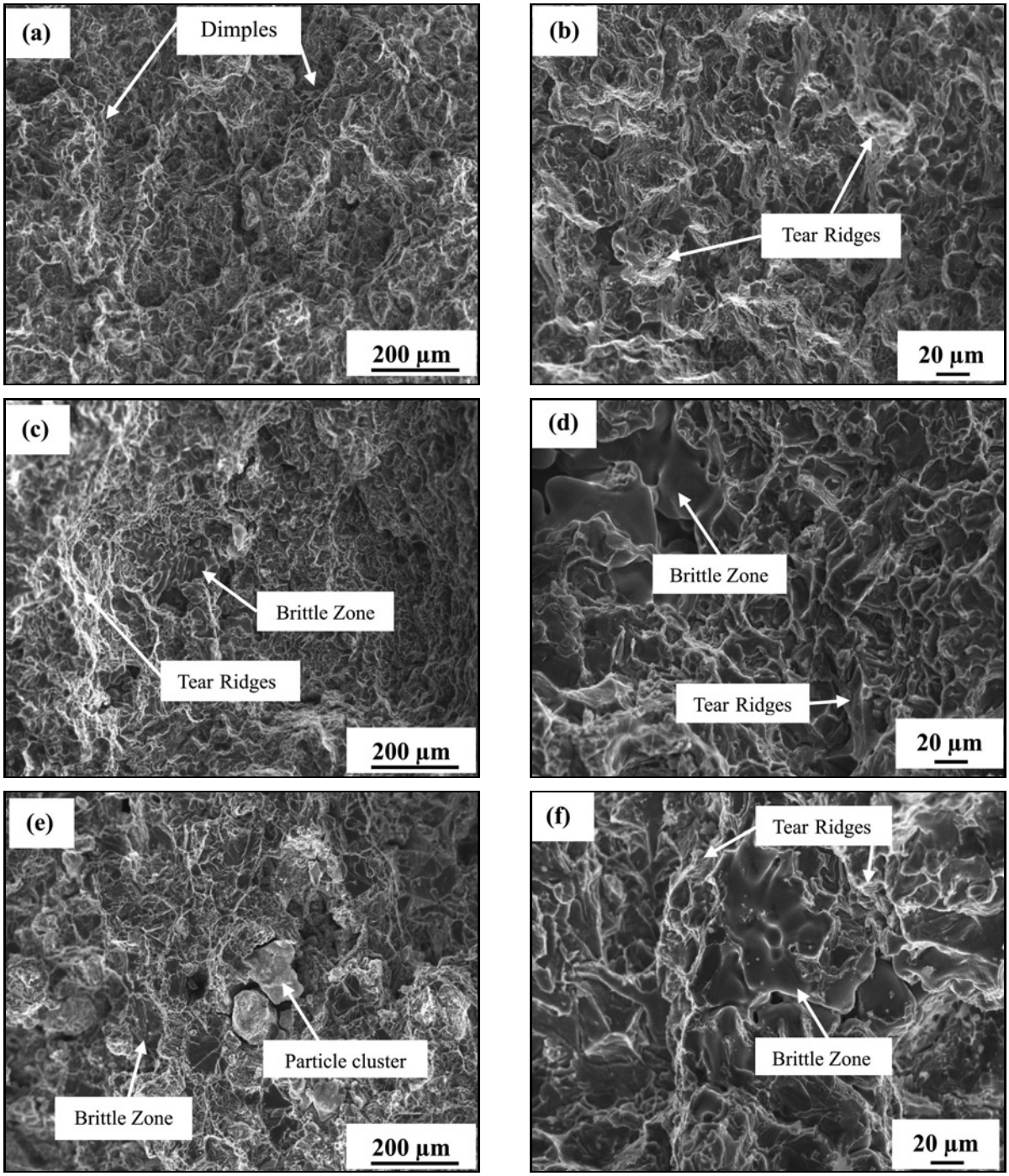

Fig. 11. Fracture surface morphology of composite samples: (a) and (b) A3; (c) and (d) A4; (e) and (f) A5.

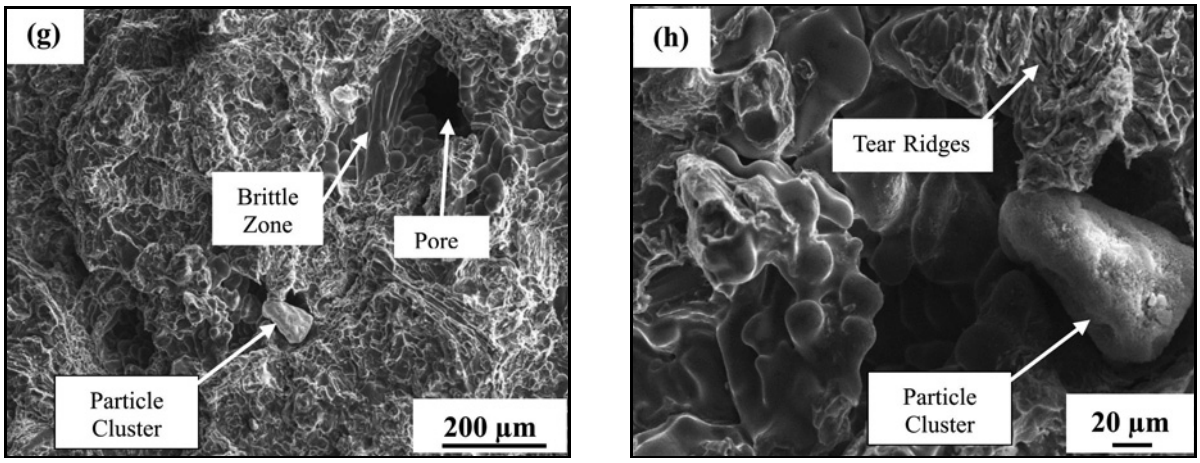

Fig. 11. Fracture surface morphology of composite samples: (g) and (h) A6.

of the fracture surface of composite samples A2, A3, and A4 support the improvement observed in ductility and tensile strength.

4.3. Workability

The composite sample A0 (monolithic alloy), sample A1 (with 7.5 wt.% Metakaolin), and sample A4 (with 1.5 wt.% Si_3N_4 and 7.5 wt.% Metakaolin) were chosen to study the effect of the hybridization in the workability of the composites. The hybrid composite sample A4 was selected among other hybrid samples as it exhibited higher compressive strength. The images of deformed composites A0, A1, and A4 and the microstructure of the surface parallel to the axis of the same samples are also shown in Fig. 12, along with the stress-strain plot.

It can be witnessed that all the stresses increased with an increase in the axial strain. The sense of the axial stress was considered negative as it was compressive, and the hoop stress was accounted in tensile nature as the cylindrical specimen bulged due to compressive load. The calculated values of mean and effective stresses were found to be compressive and tensile in nature, respectively. The hoop stress values were observed to be less compared to that of the axial stress. The mean stress possessed the lowest magnitude, and the effective stress possessed the highest values. At the initial stages of loading, all the stress components increased rapidly due to the deformation of composites. Later on, the increase in the stress components with axial strain was much slower, which is attributed to the geometrical work hardening, as reported by Mohan Raj et al. [32].

It was evident from the stress-strain plots that the hybrid composite sample required a higher load to fail under quasi-static compression and the unreinforced sample A0 failed at a lower load. The deformed surface microstructures of the sample under quasi-static compression were used to justify the variation in failure stress of the composite samples. The fracture surface of sample A0 showed numerous pores. Closed pores could also be observed, resulting from the compressive loading [12]. However, the increased amount of pores present in sample A0 caused the initiation and propagation of cracks at a lower load. The microstructure of hybrid composite sample A4 represented the closed pores and well-bonded reinforcement particles which offered resistance to the compressive loading. In addition, the microstructure of sample A4 shows a significantly less amount of pores compared to composite sample A1 with Metakaolin particles and the monolithic alloy A0. This, in turn, could be attributed to the higher failure load. From the microstructure of sample A1, a few pores, some closed pores, and well-bonded reinforcement particles were noted. The pores initiate fracture while the hard reinforcement particles resist the compressive load. Anyhow, the amount of pores in the composites reduced the resistance for compression loading compared to hybrid composite sample A4. This reason may be attributed to the intermediate failure load value of sample A1 between samples A0 and A4.

4.3.1. Instantaneous strain hardening exponent and strength coefficient

Figures 13a–d represent the variation of axial stress, hoop stress, mean stress, and effective stress with respect to axial strain, respectively. From Figs. 13a–d, it could be perceived that the amount of reinforcement particles increased all the stress components. The highest value of all the stress components in quasi-static compression was observed for sample A4. The reduction in hoop stress indicates bulging and barrelling of cylindrical samples. The hard ceramic particles in the matrix impede the dislocation motion

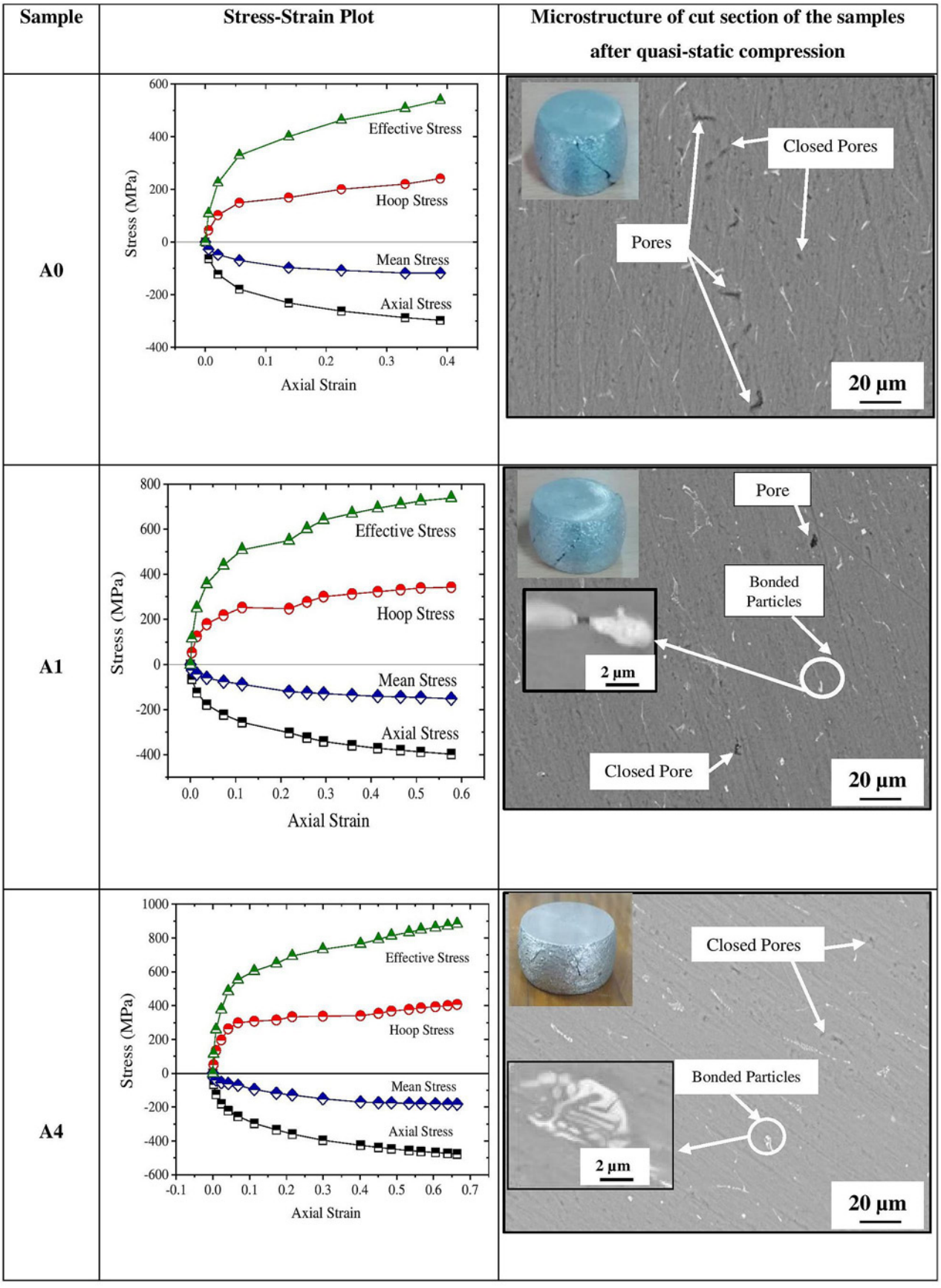

Fig. 12. Stress-strain plot and microstructure mapping of cut-section of the samples A0, A1, and A4.

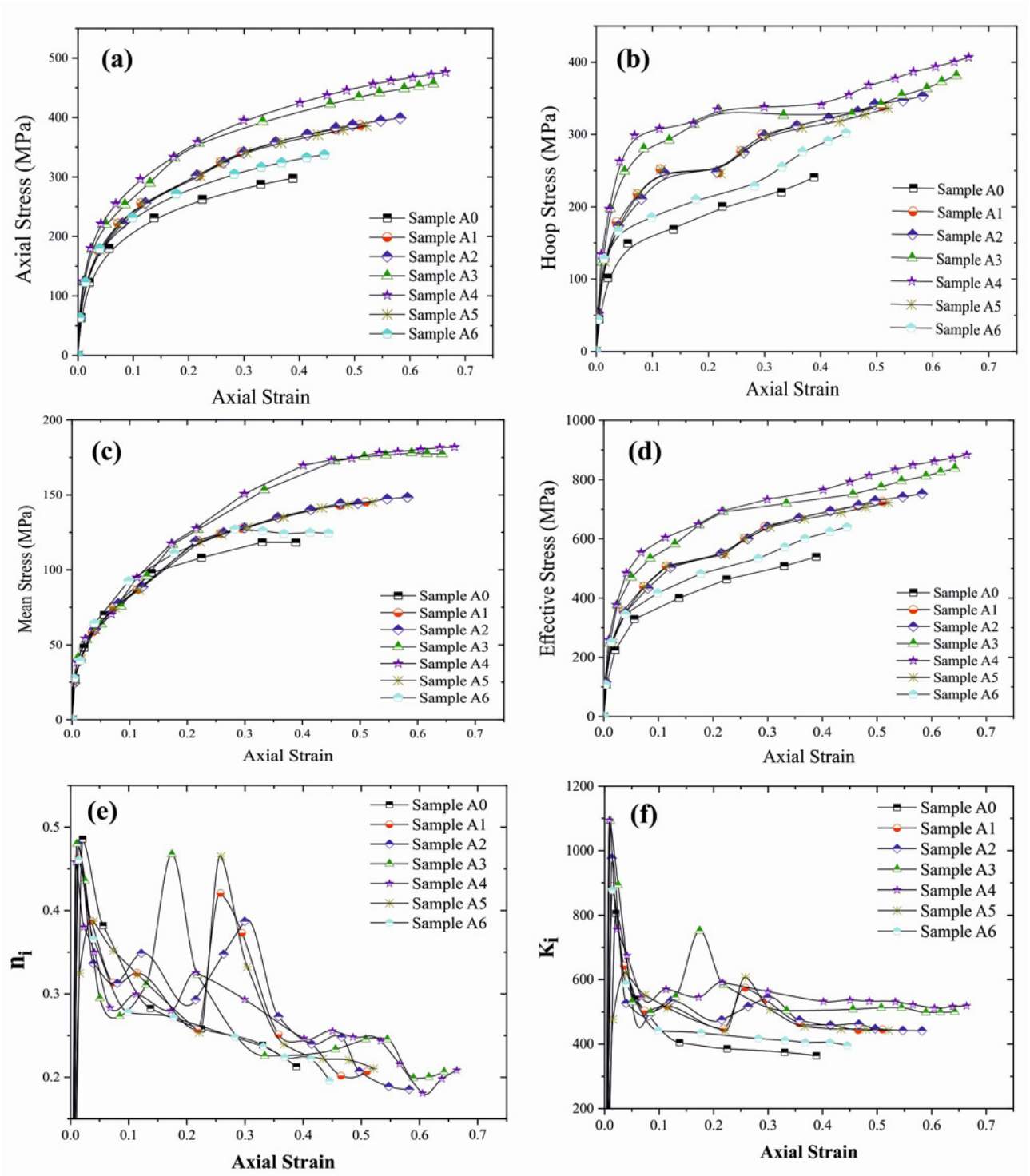

Fig. 13. Relationship between axial strain and (a) axial stress, (b) hoop stress, (c) mean stress, d) effective stress, (e) strain hardening exponent n_i, and (f) strength coefficient K_i of the composite samples.

and delay the propagation of cracks. The workability stress values of samples A5 and A6 were observed to be much lower as the crack initiated at lower compressive loads due to the presence of a high particle-porosity cluster. Monolithic sample A0 failed at the lowest values of the stresses even when the porosity levels were comparatively lower than samples A5 and A6. This result could be attributed to the absence of reinforcement particles to obstruct the propagation of cracks.

Figure 13e represents the variation of instantaneous strain hardening exponent n_i with axial strain.

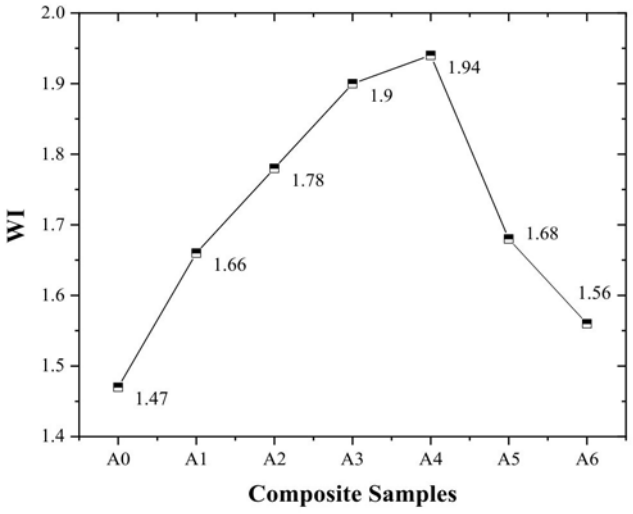

Fig. 14. Workability index WI of the composite samples.

It could be observed from Fig. 13e that the instantaneous strain hardening exponent n_i reached a higher value at the initial load and got reduced upon further loading. The initial increase may be attributed to the higher initial resistance to deformation offered by the composites due to matrix work hardening [32, 33]. On further loading, the n_i values decreased with the increase in the axial strain as the resistance to deformation is reduced due to a reduction in matrix work hardening and an increase in geometric work hardening [32, 33]. The incorporation of the reinforcement particles slightly reduced the n_i values. All the composites exhibited a secondary strain hardening characterized by the sudden increase and decrease of $n_i$values at intermediate values of the axial strain. The secondary strain hardening was attributed to the resistance to the axial compression offered by the hard reinforcement particles. However, the secondary strain hardening was found to be absent in the unreinforced AA6082 sample A0. Narayanasamy et al. [33] also observed a similar outcome. Figure 13f represents the variation of instantaneous strength coefficient K_i with respect to axial strain for all the composites. The variation of K_i values exhibited a similar attribute as that of the variation of n_i values.

4.3.2. Workability index

Figure 14 shows the variation of the workability index WI of the composite samples. The variation of WI values of the composites exhibited a similar trend as that observed in the variation of compressive strength values. The WI signifies the final height up to which the cylindrical samples could be compressed without fracture. The WI values increased with the incorporation of reinforcements in the AA6082 matrix. The composite sample A4 was observed to have the highest value of WI. Sample A3 also exhibited a similar result. It was observed that the incorporation of reinforcement particles increased the load-bearing capacity and delayed the failure. The unreinforced AA6082 sample A0 and hybrid composite sample A6 were observed to have comparatively lower WI values. The samples A0 and A6 failed at a lower load without being compressed much due to the existence of pores. The absence of reinforcements in sample A0 and the presence of an increased amount of particle-porosity cluster in sample A6 might have triggered the failure of A0 and A6 at a lower load and lesser deformed height.

5. Conclusions

The AA6082 hybrid composites with Metakaolin and nano-Si_3N_4 particles were synthesized successfully using the ultrasonication-assisted stir casting process. The reinforcement particles were subjected to a premixing process before embedding in the matrix. The microstructure of the prepared composites represented uniform dispersion of the reinforcement particles in the AA6082 matrix up to the addition of 1 wt.% of Si_3N_4 nanoparticles. Grain refinement spots were also noticed for the hybrid composite with 1 wt.% Si_3N_4 nanoparticle. Incorporating nano Si_3N_4 particles in the AA6082 matrix improved the strength of the composites without compromising the ductility. However, while the Si_3N_4 particles were added beyond 1 wt.%, the formation of particle-porosity clusters started to increase. Large particle clusters were observed for the composite samples A5 and A6 with 2 wt.% and 2.5 wt.% Si_3N_4 reinforcements, respectively. The analysis of the tensile fracture surface revealed the occurrence of mixed-mode of ductile and brittle fracture. Primary strengthening mechanisms were observed as strengthening due to the dispersion of reinforcements and grain refinement.

The compressive strength of the composites also improved with the increase in the incorporation of nano Si_3N_4 reinforcements. The composite A4 with 1.5 wt.% Si_3N_4 possessed the best compressive strength among the composites. Conversely, the tensile strength was lower, and the porosity was higher for composite sample A4. The pore closure phenomenon was supposed to increase the compressive strength of sample A4. The workability behaviour of the composites was studied by performing quasi-static compression. The stress components related to quasi-static compression were higher for hybrid composites with Si_3N_4 reinforcements. The increase in load-bearing capacity in hybrid composites was the reason for the increased values of the stresses. The strain hardening behaviour of the composites was analysed by computing

the instantaneous strain hardening exponent and instantaneous strength coefficient. The particle-porosity cluster significantly affected the strain hardening phenomena and the workability of the composites. The hybrid composites possessed higher workability index values.

References

[1] R. J. Bright, G. Selvakumar, M. Sumathi, Prediction of dry sliding wear behaviour of China clay particles reinforced AA6082 matrix composites using response surface methodology and analysis of the worn surfaces, Surf. Topogr.: Metrol. Prop. 10 (2022) 015037. https://doi.org/10.1088/2051-672X/ac59d4

[2] J. David Raja Selvam, D. S. Robinson Smart, I. Dinaharan, Microstructure and some mechanical properties of fly ash particulate reinforced AA6061 aluminum alloy composites prepared by compocasting, Mater. Des. 49 (2013) 28–34. https://doi.org/10.1016/j.matdes.2013.01.053

[3] M. Oluwatosin Bodunrin, K. Kanayo Alaneme, L. H. Chown, Aluminium matrix hybrid composites: a review of reinforcement philosophies; Mechanical, corrosion and tribological characteristics, J. Mater. Res. Technol. 4 (2015) 434–445. https://doi.org/10.1016/j.jmrt.2015.05.003

[4] K. Kanayo Alaneme, B. J. Bamike, Characterization of mechanical and wear properties of aluminium based composites reinforced with quarry dust and silicon carbide, Ain Shams Eng. J. 9 (2018) 2815–2821. https://doi.org/10.1016/j.asej.2017.10.009

[5] Uppada Rama Kanth, Putti Srinivasa Rao, M. G. Krishna, Mechanical behaviour of fly ash/SiC particles reinforced Al-Zn alloy-based metal matrix composites fabricated by stir casting method, J. Mater. Res. Technol. 8 (2019) 737–744. https://doi.org/10.1016/j.jmrt.2018.06.003

[6] S. M. Quader, B. Suryanarayana Murthy, P. Ravinder Reddy, Processing and mechanical properties of Al_2O_3 and red mud particle reinforced AA6061 hybrid composites, J. Miner. Mater. Charact. Eng. 4 (2016) 135–142. https://doi.org/10.4236/jmmce.2016.42013

[7] B. Praveen Kumar, A. Kumar Birru, Characterization of Al-4.5%Cu alloy with the addition of silicon carbide and bamboo leaf ash, Kovove Mater. 56 (2018) 325–337. https://doi.org/10.4149/km_2018_5_325

[8] J. Zhu, W. Jiang, G. Li, F. Guan, Y. Yu, Z. Fan, Microstructure and mechanical properties of SiC_{np}/Al6082 aluminum matrix composites prepared by squeeze casting combined with stir casting, J. Mater. Process. Tech. 283 (2020) 116699. https://doi.org/10.1016/j.jmatprotec.2020.116699

[9] X. Yang, N. S. Barekar, S. Ji, B. K. Dhindaw, Z. Fan, Influence of reinforcing particle distribution on the casting characteristics of Al-SiCp composites, J. Mater. Process. Tech. 279 (2020) 116580. https://doi.org/10.1016/j.jmatprotec.2019.116580

[10] S. R. Wang, H. R. Geng, Y. Z. Wang, J. C. Zhang, Microstructure and fracture characteristic of Mg-Al-Zn--Si_3N_4 composites, Theor. Appl. Fract. Mech. 46 (2006) 57–69. https://doi.org/10.1016/j.tafmec.2006.05.005

[11] M. R. Mattli, P. R. Matli, A. Shakoor, A. M. Amer Mohamed, Structural and mechanical properties of amorphous Si_3N_4 nanoparticles reinforced Al matrix composites prepared by microwave sintering, Ceramics 2 (2019) 126–134. https://doi.org/10.3390/ceramics2010012

[12] P. Hariharasakthisudhan, S. Jose, Influence of metal powder premixing on mechanical behavior of dual reinforcement (Al_2O_3 (μm)/Si_3N_4(nm)) in AA6061 matrix, J. Alloys Compd. 731 (2018) 100–110. https://doi.org/10.1016/j.jallcom.2017.10.002

[13] H. Arik, Effect of mechanical alloying process on mechanical properties of α-Si_3N_4 reinforced aluminum-based composite materials, Mater. Des. 29 (2008) 1856–1861. https://doi.org/10.1016/j.matdes.2008.03.010

[14] Z. Zhang, D. L. Chen, Consideration of Orowan strengthening effect in particulate-reinforced metal matrix nanocomposites: A model for predicting their yield strength, Scr. Mater. 54 (2006) 1321–1326. https://doi.org/10.1016/j.scriptamat.2005.12.017

[15] D. Yuan, X. Yang, S. Wu, S. Lü, K. Hu, Development of high strength and toughness nano-SiCp/A356 composites with ultrasonic vibration and squeeze casting, J. Mater. Process. Technol. 269 (2019) 1–9. https://doi.org/10.1016/j.jmatprotec.2019.01.021

[16] L. Poovazhagan, K. Kalaichelvan, T. Sornakumar, Processing and performance characteristics of aluminum-nano boron carbide metal matrix nanocomposites, Mater. Manuf. Process. 31 (2016) 1275–1285. https://doi.org/10.1080/10426914.2015.1026354

[17] C. Kannan, R. Ramanujam, Effectiveness evaluation of molten salt processing and ultrasonic cavitation techniques during the production of aluminium based hybrid nanocomposites – An experimental investigation, J. Alloys Compd. 751 (2018) 183–193. https://doi.org/10.1016/j.jallcom.2018.04.112

[18] R. Harichandran, N. Selvakumar, Microstructure and mechanical characterization of (B_4C+ h-BN)/Al hybrid nanocomposites processed by ultrasound assisted casting, Int. J. Mech. Sci. 144 (2018) 814–826. https://doi.org/10.1016/j.ijmecsci.2017.08.039

[19] R. Narayanasamy, T. Ramesh, K. S. Pandey, Workability studies on cold upsetting of Al-Al_2O_3 composite material, Mater. Des. 27 (2006) 566–575. https://doi.org/10.1016/j.matdes.2004.12.005

[20] R. Narayanasamy, T. Ramesh, M. Prabhakar, Effect of particle size of SiC in aluminium matrix on workability and strain hardening behaviour of P/M composite, Mater. Sci. Eng. A 504 (2009) 13–23. https://doi.org/10.1016/j.msea.2008.11.037

[21] M. A. Taha, N. A. El-Mahallawy, A. M. El-Sabbagh, Some experimental data on workability of aluminium-particulate-reinforced metal matrix composites, J. Mater. Process. Technol. 202 (2008) 380–385. https://doi.org/10.1016/j.jmatprotec.2007.07.047

[22] R. J. Bright, G. Selvakumar, M. Sumathi, N. Lenin, Development, mechanical characterization and analysis of dry sliding wear behavior of AA6082-Metakaolin metal matrix composites, Mater. Res. Express 6 (2019) 126516. https://doi.org/10.1088/2053-1591/ab52aa

[23] R. Narayanasamy, K. S. Pandey, Phenomenon of barrelling in aluminium solid cylinders during cold upset-forming, J. Mater. Process. Technol. 70 (1997) 17–21. https://doi.org/10.1016/S0924-0136(97)00035-6
[24] M. Abdel-Rahman, M. N. El-Sheikh, Workability in forging of powder metallurgy compacts, J. Mater. Process. Tech. 54 (1995) 97–102. https://doi.org/10.1016/0924-0136(95)01926-X
[25] K. Logesh, P. Hariharasakthisudhan, A. Arul Marcel Moshi, B. Surya Rajan, K. Sathickbasha, Mechanical properties and microstructure of A356 alloy reinforced AlN/MWCNT/graphite/Al composites fabricated by stir casting, Mater. Res. Express 7 (2020) 015004. https://doi.org/10.1088/2053-1591/ab587d
[26] D. Zhou, F. Qiu, Q. Jiang, Simultaneously increasing the strength and ductility of nano-sized TiN particle reinforced Al-Cu matrix composites, Mater. Sci. Eng. A 596 (2014) 98–102. https://doi.org/10.1016/j.msea.2013.12.049
[27] P. N. Bindumadhavan, Heng Keng Wah, O. Prabhakar, Dual particle size (DPS) composites: Effect on wear and mechanical properties of particulate metal matrix composites, Wear 248 (2001) 112–120. https://doi.org/10.1016/S0043-1648(00)00546-9
[28] N. Panwar, A. Chauhan, Parametric behaviour optimisation of macro and micro hardness for heat treated Al 6061-red mud composite, J. Mater. Res. Technol. 8 (2019) 660–669. https://doi.org/10.1016/j.jmrt.2018.04.018
[29] R. Raj, D. G. Thakur, Effect of particle size and volume fraction on the strengthening mechanisms of boron carbide reinforced aluminum metal matrix composites, Proc. Inst. Mech. Eng. Part C J. Mech. Eng. Sci. 233 (2019) 1345–1356. https://doi.org/10.1177/0954406218771997
[30] T. Xu, G. Li, M. Xie, M. Liu, D. Zhang, Y. Zhao, G. Chen, X. Kai, Microstructure and mechanical properties of in-situ nano γ-Al_2O_3p/A356 aluminum matrix composite, J. Alloys Compd. 787 (2019) 72–85. https://doi.org/10.1016/j.jallcom.2019.02.045
[31] J. A. K. Gladston, N. Mohamed Sheriff, I. Dinaharan, J. D. Raja Selvam, Production and characterization of rich husk ash particulate reinforced AA6061 aluminum alloy composites by compocasting, Trans. Nonferrous Met. Soc. China 25 (2015) 683–691. https://doi.org/10.1016/S1003-6326(15)63653-6
[32] A. P. Mohan Raj, N. Selvakumar, R. Narayanasamy, C. Kailasanathan, Experimental investigation on workability and strain hardening behaviour of Fe-C--Mn sintered composites with different percentage of carbon and manganese content, Mater. Des. 49 (2013) 791–801. https://doi.org/10.1016/j.matdes.2013.02.002
[33] R. Narayanasamy, N. Selvakumar, K. S. Pandey, Phenomenon of instantaneous strain hardening behaviour of sintered Al-Fe composite preforms during cold axial forming, Mater. Des. 28 (2007) 1358–1363. https://doi.org/10.1016/j.matdes.2006.01.020